Ridged Apertures for LEO Direct Radiating Arrays in Ka-Band

applied sciences

MDPI

Article

Ridged Apertures for LEO Direct Radiating Arrays in Ka-Band

Carlos Vazquez-Sogorb *, Roger Montoya-Roca, Giuseppe Addamo, Oscar Antonio Peverini and Giuseppe Virone

IEIIT, National Research Council of Italy—CNR, 10129 Turin, Italy; roger.montoyaroca@ieiit.cnr.it (R.M.-R.); giuseppe.addamo@ieiit.cnr.it (G.A.); oscar.peverini@ieiit.cnr.it (O.A.P.); giuseppe.virone@cnr.it (G.V.)
* Correspondence: carlos.vazquezsogorb@ieiit.cnr.it

Abstract: This paper presents an extensive performance analysis of open-ended waveguide elements for direct radiating arrays with a high scan angle (±50°/60°). The evaluated designs are based on square and hexagonal apertures loaded with ridges. Both square and triangular lattices are considered in the framework of Ka-band downlink design requirements for future LEO mega-constellations. The parameter space defined by the monomodal condition has been explored to find an optimum value for each structure. The analyses carried out with both infinite and finite full-wave models in terms of active reflection coefficient, scan loss and cross-polar discrimination are in good agreement.

Keywords: open-ended waveguide; direct radiating array; LEO satellite; satellite communication; non-terrestrial networks; Ka-band; phased array antenna

Citation: Vazquez-Sogorb, C.; Montoya-Roca, R.; Addamo, G.; Peverini, O.A.; Virone, G. Ridged Apertures for LEO Direct Radiating Arrays in Ka-Band. *Appl. Sci.* **2024**, *14*, 7825. https://doi.org/10.3390/app14177825

Academic Editor: Paulo M. Mendes

Received: 28 June 2024
Revised: 31 July 2024
Accepted: 6 August 2024
Published: 3 September 2024

1. Introduction

The new generation 6G paradigm is expected to offer uninterrupted connectivity and coverage everywhere through non-terrestrial networks (NTN). The key aspect is the usage of satellite communications (SatCom) to complement the terrestrial networks in both fixed and mobile scenarios (SatCom on the move). To this end, low Earth orbit (LEO) satellites are the most promising solution in terms of lower attenuation and smaller latency [1] compared to medium Earth orbit or geostationary orbit satellites.

Nowadays, a SatCom user link generally operates at Ku- and Ka-bands. Multibeam antennas are required to send the information to different spots on the Earth, maximizing spatial diversity and covering wide areas [1,2]. At LEO, direct radiating array (DRA) antennas are a suitable candidate for flexible multibeam operation. However, a significant scan range of ±50°/60° is required [3,4], which is a challenging aspect of antenna design in terms of impedance matching and polarization purity. Other important figures of merit are radiation efficiency, cost and weight.

Within this framework, a few radiating elements have been presented in the literature, such as waveguide apertures (open-ended waveguides) [5–7], Vivaldi [8,9], microstrip patch [10,11] and substrated integrated waveguide (SIW) antennas [12]. Among the different solutions, all-metal ones are promising thanks to their good power handling capabilities and higher radiation efficiency. An all-metal evanescent quadridge antenna (EQA, square waveguide loaded with four ridges [13,14]) operating in the Ku-band has been proposed in [5]. The antenna works in a 4.5% bandwidth with good performance up to a ±50° scanning angle. Unfortunately, this design does not cover the full downlink Ka-band (17.7–20.2 GHz), where the bandwidth is 13.2%. Waveguide-based and all-metal Vivaldi radiating elements covering the full Ka-band are presented in [15,16]. The first one provides low performance at the E-plane, where a ±60° scan blindness appears at 20 GHz. Concerning the all-metal Vivaldi radiating element, both E- and H-planes provide good performance when they scan up to ±40° with an active reflection coefficient (ARC) lower than −10 dB. Instead, Circular polarization is difficult to achieve with such Vivaldi arrays.

In this paper, we provide an extensive study of ridged apertures (i.e., open-ended ridge waveguides) to assess their performance as array elements. We present results for square and hexagonal waveguides in square [14] and triangular lattices [17,18], respectively (such geometries are sketched out in Figure 1). Differently from [5], we only consider the element at the aperture level, i.e., without the matching section in order to find the intrinsic peculiarities and limitations of each configuration. In this way, this study offers a starting point to design more complex elements integrating element as well as cascaded discontinuities to match improvement and polarization conversion.

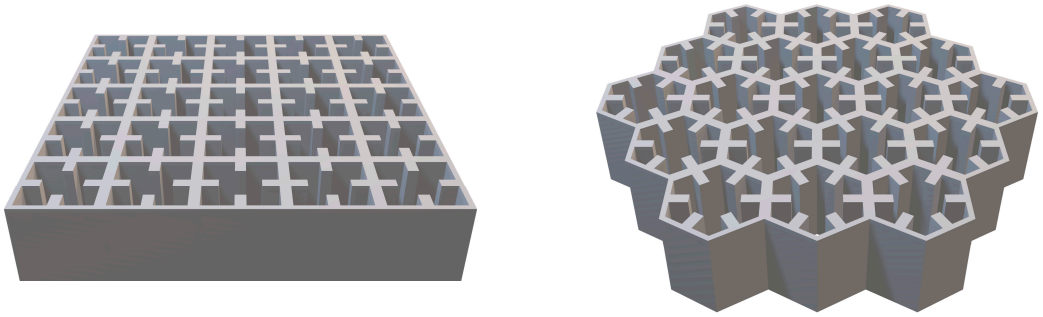

(**a**) Square lattice (**b**) Triangular lattice

Figure 1. Open-ended ridged waveguide elements in square and triangular lattices.

The novelty aspect of this paper is the study of square and hexagonal ridged waveguides in an array environment covering a bandwidth of 13.2%, i.e., the downlink Ka-band in terms of ARC, scan loss and cross-polar discrimination (XPD). For all configurations, we provide cut-off, parametric and complete performance analyses for the optimum parameter sets using both linear and circular polarization. Even if the system operates using circular polarization, linear polarization provides additional physical insights, i.e., it clearly shows that the reduced performance at high-scan angles is due to the scan blindness phenomena.

All the optimum geometrical parameters are reported as a reference for future design activities. The provided cut-off and parametric analyses can be used as design curves to investigate different operative frequencies and manufacturing constraints.

To the best of the author's knowledge, this is the first paper showing the performance of the quadridge element within a 13.2% bandwidth up to a $\pm 60^{\circ}$ scan angle. This is also the first paper providing results on a hexagonal ridged waveguide in a triangular lattice to overcome the limits of quadridge.

The paper is organized as follows: Section 2 describes the main parameters for a LEO array design, such as periodicity and configuration. Section 3 presents the cut-off analyses for both quadridge and hexagonal waveguides. Section 4 discusses and compares the performance of the proposed radiating elements in terms of S-Parameters, scan loss and XPD. Section 5 validates the results using both infinite and finite array approaches. The conclusion is reported in Section 6.

2. Array Design for LEO

As far as antennas for LEO satellites are concerned, typical requirements for array gain are in the order of 35 dBi. Considering an element gain of 6 dBi with a scan loss of 3 dB at the maximum scan angle, the resulting number of elements is in the order of 48×48 elements. The inter-element spacing providing a grating lobe-free condition is defined in Equation (1) [19,20].

$$\frac{p}{\lambda} \leq \frac{1}{sin\theta_{L,i}} \frac{1 - \frac{1}{N}}{1 + sin\theta_S} \tag{1}$$

where $\theta_{L,i}$ defines the lattice angle (i.e., see Figure 2, $\theta_{L,1} = 90°$ for the square lattice and $\theta_{L,2} = 60°$ for the triangular lattice), θ_S is the maximum scan angle and N is the number of elements in a row/column.

(**a**) Square lattice (**b**) Triangular lattice

Figure 2. Lattice geometry.

According to Equation (1) and considering both the highest frequency of the band (20.2 GHz) and a scan limit of 60°, the period is equal to 7.8 mm ($p = 0.52\lambda$) and 9 mm ($p = 0.61\lambda$) for the square (Figure 2a) and triangular lattices (Figure 2b), respectively. Both arrangements are studied in this paper.

The array period reported above have been computed considering a finite array approach, which is suitable for a future prototype. Nevertheless, the large number of elements, i.e., 48 × 48, justifies an infinite array approach for the element design.

3. Waveguide Design: Cut-Off Analyses

The array period was computed in the previous section to satisfy the grating lobe-free condition. With reference to Figure 1, waveguides should be smaller than the array period ($a < p$) to provide a minimum metal thickness of 1 mm for manufacturability [21]. Therefore, the maximum waveguide sizes a are 6.8 mm and 8 mm for square and triangular lattices, respectively. Such sizes do not allow fundamental degenerate mode propagation in the operative band if square or circular/hexagonal waveguides are considered (cut-off frequencies would be about 22 GHz, preventing signal propagation from input port to the aperture in the operative frequency band), e.g., $f_c = c_{light}/2a$ in the square waveguide. Dielectric filling has been proposed in [7] to lower the cut-off frequencies of such waveguides. Similarly to [5], in this work we instead propose the use of ridges to achieve fundamental mode propagation in the frequency band together with low losses (all-metal solutions) and easier manufacturing. When ridges are loaded into the waveguide, they effectively change the boundary conditions and the distribution of the electromagnetic fields. As can be seen in [22,23] this significantly reduces the cut-off frequency of the fundamental modes ($f_c < c_{light}/2a$) without significant variation of the higher-order modes, leading to an overall increase in bandwidth.

All-metal antennas are also generally preferred for space applications [24]. New manufacturing techniques such as Additive Manufacturing help not only to manufacture complex metal structures in one piece, but also to reduce the amount of material where it is not needed. In this way, the overall mass can be reduced without affecting performance. Metal structures provide better thermal performance in terms of higher dissipation and lower deformation. The absence of dielectrics also leads to better radiation efficiency (no dielectric losses).

The design of the ridged waveguides in terms of cut-off frequencies are reported in the next subsections. Such non-canonical waveguides [22,23] require a numerical approach to be evaluated. We adopted the mode solver of the CST Microwave Studio mode solver [25] in the present study.

All the waveguides reported in the next sections will support two orthogonal degenerate modes (two modes having the same cut-off frequency and hence the same propagation constant). This feature is needed to avoid deterioration of circularly polarized signals. Circular polarization in a waveguide is indeed a combination of two orthogonal linearly

polarized modes whose phase difference of 90° (as excited by the polarizer [26]) should remain constant during propagation in the waveguide.

3.1. Quadridge Waveguide

The geometry of the quadridge waveguide [13,14] and its parameters can be seen in Figure 3. As written above, the waveguide's side a is 6.8 mm. The iso-level curves of the cut-off frequencies for the two fundamental degenerate modes $f_{c_{1,2}}$ and the higher-order mode f_{c_3} are shown in Figure 4a,b, respectively, as a function of the width w_R and the height h_R of the ridges. Even if the waveguide supports two degenerate modes (one for each polarization) the intervals $f_{c_{1,2}}$ and f_{c_3} can be referred to as monomodal bandwidths.

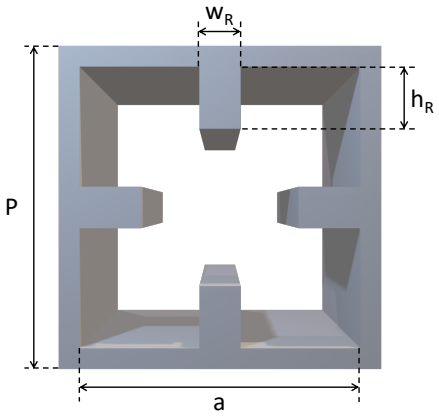

Figure 3. Proposed quadridge waveguide aperture for square lattice array.

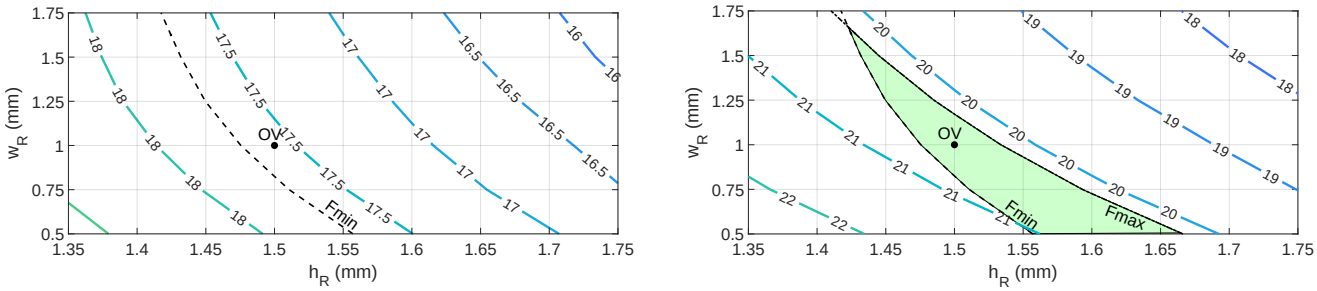

(**a**) Quadridge (degenerate Mode 1 & 2) (**b**) Quadridge (Mode 3)

Figure 4. Cut-off frequency map for the quadridge waveguide. The green region indicates all possible valid solutions for the operative bandwidth. The point labelled OV refers to the optimal value based on both the manufacturing constraints and equal spacing between the frequency limits for Fmin and Fmax (see Section 4.1).

The dashed line corresponds to the lower limit of the operative bandwidth ($F_{min} = 17.7$ GHz). Therefore, the useful ridge parameter combinations is on the right-hand side of Figure 4a ($f_{c_{1,2}} < F_{min}$). On the other hand, the dash-dotted line in Figure 4b shows the upper limit of the operative bandwidth ($F_{max} = 20.2$ GHz). The dashed curve is reported again in Figure 4b to obtain the parameter region where only the two fundamental degenerate modes are propagating within the frequency band (17.7–20.2 GHz). It can be seen that low values of w_R provide a larger available range of ridge height, h_R. However, such regions should be further reduced considering a manufacturing constraint of 1 mm for the minimum ridge width. An optimal value (OV) has been chosen to be almost equally spaced from both cut-off frequency limits. The resulting dimensions are h_R equal to 1.5 mm and w_R equal to 1 mm, providing a cut-off frequency of 17.6 GHz (see Figure 4a) for the fundamental degenerate modes $f_{c_{1,2}}$ and 20.5 GHz (see Figure 4b) for the third mode f_{c_3}. The performance of this waveguide as a radiating element will be shown in Section 4.1.

From the previous analysis, it is apparent that the quadridge configuration does not provide large margins between the operative band and the corresponding cut-off frequencies. This is consistent with the significant bandwidth limitations for this type of element shown in Section 4.1. For this reason, the hexagonal waveguide with three and six ridges is studied in the next subsection. It should be noted that Figure 4a,b can be also used to perform the design of quadridge waveguides with different operative frequencies (not necessarily Ka downlink). The reported cut-off data allow for a wider combination of parameters.

The electrical field distribution for the two fundamental degenerate modes (Mode 1 and Mode 2) and the higher-order mode (Mode 3) of the quadridge are shown in Figure 5 [27]. The electrical field distribution is computed using CST Studio Suite 2021 instead of alternative numerical codes for ridge waveguides [28]. Because the aperture has two-fold symmetry, the first two modes have the same propagation constant, also called degenerate modes (the first mode is aligned along the horizontal axis, Figure 5a, while the second mode is on the vertical axis, Figure 5b).

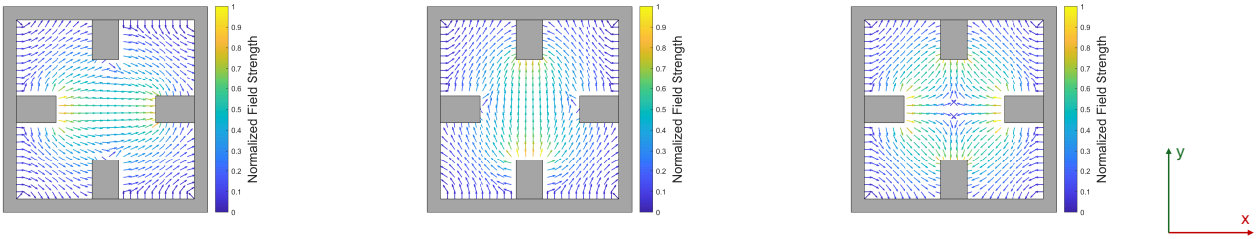

(**a**) Mode 1 (**b**) Mode 2 (**c**) Mode 3

Figure 5. Electrical field distribution for the quadridge modes.

3.2. Hexagonal Ridged Waveguides

Hexagonal designs are presented to overcome the limitations found in the quadridge structure. Although in triangular lattice the inter-element spacing and the dimensions of the waveguide are larger than in the previous case, it is still necessary to load with ridges. The larger size of the hexagonal waveguide with respect to the quadridge is also helpful as far as manufacturing is concerned. Two configurations have been considered with three [29] and six ridges [18] (Figure 6). The former (three ridges) leads to a simple manufacturing process, whereas better polarization performance is expected from the latter (six ridges) due to its two-fold symmetry.

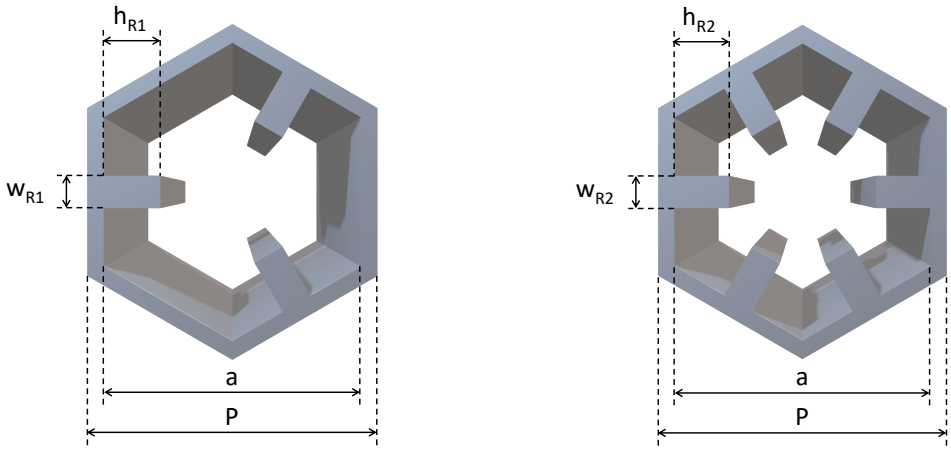

(**a**) Three ridges (**b**) Six ridges

Figure 6. Proposed hexagonal ridged apertures for triangular lattice array.

As reported in Section 2, the waveguide size a is 8 mm. The iso-level curves of the cut-off frequencies for the two fundamental degenerate modes $f_{c_{1,2}}$ and the higher-order mode f_{c_3} are shown in Figure 7, as a function of the width w_R and the height h_R of the ridges.

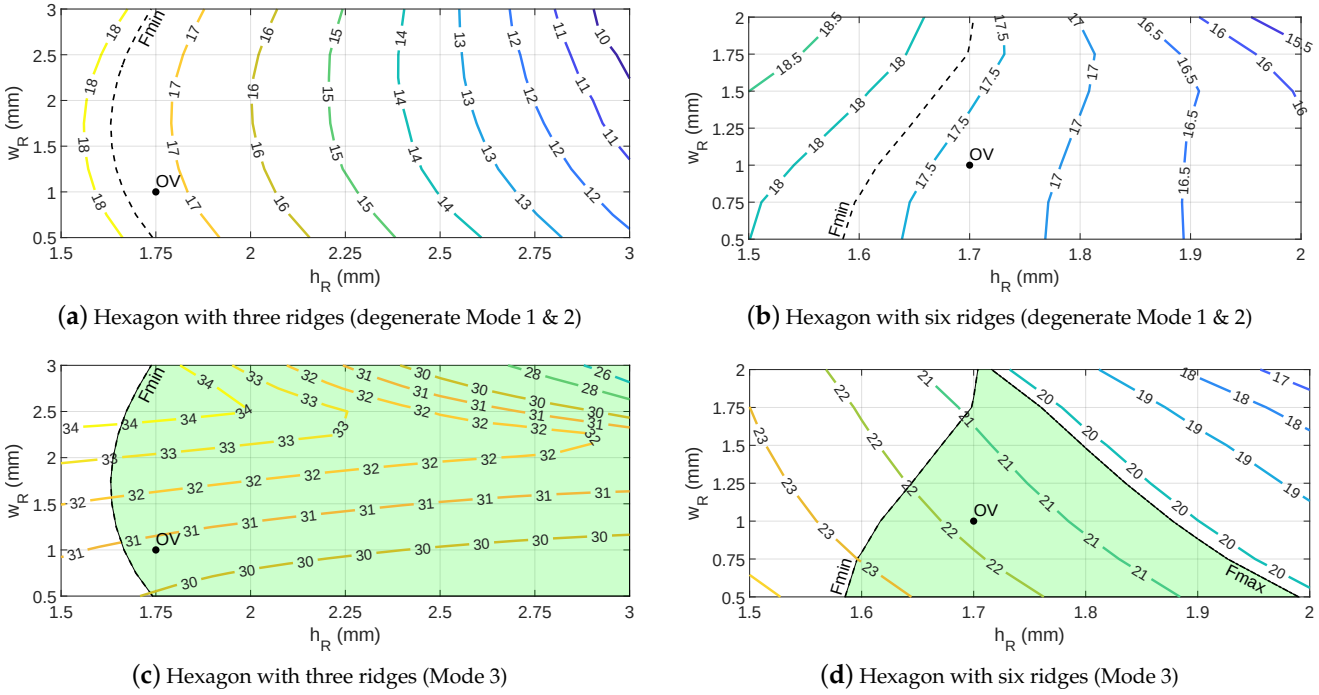

(**a**) Hexagon with three ridges (degenerate Mode 1 & 2)

(**b**) Hexagon with six ridges (degenerate Mode 1 & 2)

(**c**) Hexagon with three ridges (Mode 3)

(**d**) Hexagon with six ridges (Mode 3)

Figure 7. Cut-off frequency map for the hexagonal waveguide. The green region indicates all possible valid solutions for the operative bandwidth. The point labelled OV refers to the optimal value based on the manufacturing constraints and the radiating performance reported in Section 4.2 .

As far as the three-ridged waveguide is concerned (Figure 7a,c), it can be seen that with a parameter combination of $w_R = 2.5$ mm and $h_R = 3$ mm (close to the upper-right corner) the maximum bandwidth approaches 3:1. Therefore, in principle this waveguide can cover both a Ka-band downlink (17.7–20.2 GHz) and Ku-band downlink (10.7–12.75 GHz). This aspect again highlights the importance of the cut-off analyses in Figure 7 as design curves for future design activities.

The dashed line corresponds to the lower limit of the operative bandwidth ($F_{min} = 17.7$ GHz). Therefore, the useful ridge parameter combinations are on the right-hand side of Figure 7 ($f_{c_{1,2}} < F_{min}$).The dash-dotted line showing the upper limit ($F_{max} = 20.2$ GHz) is only visible in Figure 7d for the six-ridge configuration. As mentioned above, the three ridges do not provide limitations related to the higher-order mode ($f_{c_3} > F_{max}$ for all the considered parameter values). The benefits of the triangular symmetry (60° rotational symmetry) in terms of very high cut-off frequencies/resonances for the higher-order mode are also used in [30].

It is apparent that both solutions in Figure 6 allow for a larger range of parameters w_R and h_R with respect to the quadridge (see Figure 4). In this case, the optimal value (OV) has been determined using the full-wave simulations presented in Section 4.2.

The electrical field distributions for the two fundamental degenerate modes (Mode 1 and Mode 2) and the higher-order mode (Mode 3) of the hexagonal waveguides with three and six ridges are shown in Figure 8. The hexagonal geometry with three ridges does not have two-fold symmetry. However, the two fundamental modes (1 and 2) have the same propagation constant (Figure 8a,b). The reason for such a degeneration is shown in Figure 9. It should be noted that Mode 2 (whose field configuration in Figure 8b looks quite different from the field configuration for Mode 1 in Figure 8a) can be expressed as the difference between two 120°—rotated versions of Mode 1 (titled 1′ and 1″). It can also be shown that Mode 1 can instead be expressed as the sum of 1′ and 1″. In conclusion, all the presented

field configurations arise from 120° rotations of the same mode (or a combination of them), therefore, they have the same propagation constant (degenerate modes). Of course, any other linear combinations of the degenerate modes are possible. However, we selected Mode 1 and Mode 2 in Figure 8a,b because their E-fields are polarized along the two principal axes of our reference system (x and y) and can be easily compared to the ones of the quadridge structure. Similar considerations apply for the hexagon with six ridges, for which the field modes are shown in Figure 8d–f. Their distribution is actually closer to the quadridge waveguide due to their two-fold symmetry.

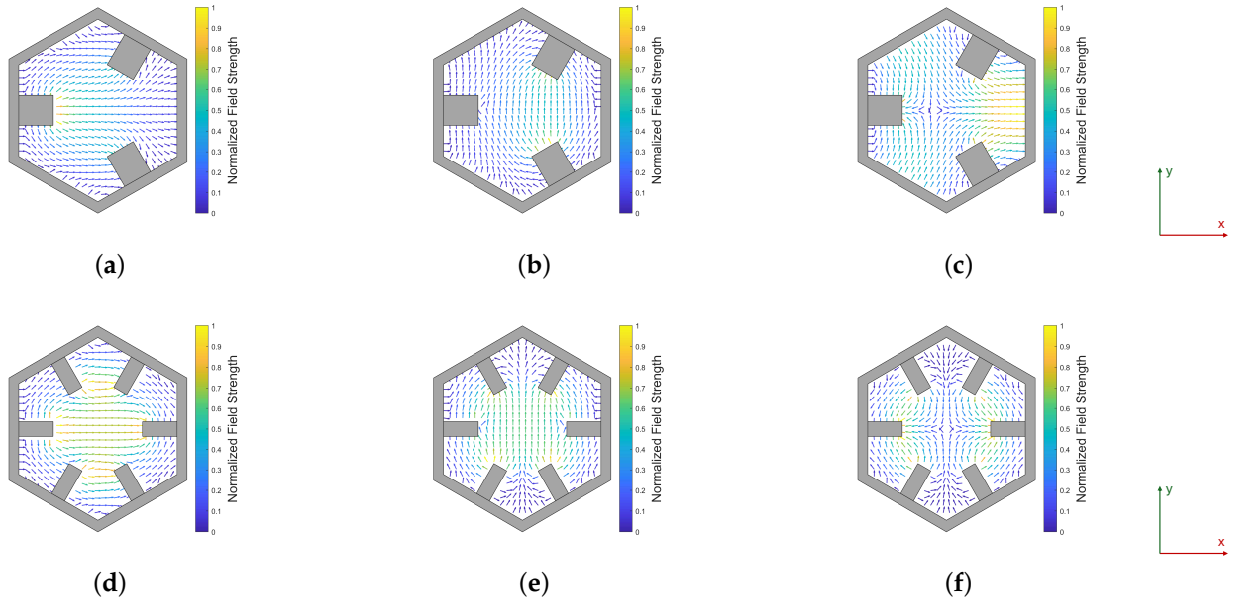

Figure 8. Electrical field distribution for the hexagonal waveguide modes. (**a**) Hexagon with three ridges (Mode 1); (**b**) hexagon with three ridges (Mode 2); (**c**) hexagon with three ridges (Mode 3); (**d**) hexagon with six ridges (Mode 1); (**e**) hexagon with six ridges (Mode 2); (**f**) hexagon with six ridges (Mode 3).

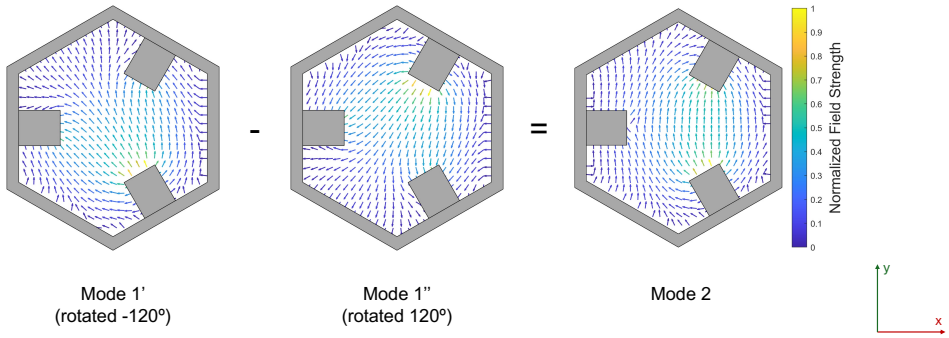

Figure 9. Degeneration modes in a three-ridged waveguide mode.

Comparing the electric field distribution between the two hexagonal apertures, we should expect symmetrical scan loss and XPD (with respect to the broadside) and higher polarization purity (see Section 4.2) for the six-ridge configuration due to its two-fold symmetry. However, it should be mentioned that XPD performance is due to a combination of modes in the aperture (modes are coupled at the discontinuity between waveguide and free-space), such a performance is rigorously evaluated using the provided XPD plots.

4. Aperture Design: Parametric Analyses and Performance Evaluation

The results shown in this section were obtained with an infinite array approach. In particular, the unit cell boundary conditions in the CST software were used to limit the numerical analysis to only one array element. The phase shift between the unit cell boundaries was automatically adjusted to achieve the required scan angles. We used a waveguide excitation with two fundamental degenerate modes and a Floquet port with 18 modes at 4.40 mm from the aperture ($0.25\lambda_0$ at 17 GHz) to efficiently absorb the radiated fields. Such an analysis model mimics an infinite array, properly excited with a beamforming network (BFN) (only phase gradients, uniform amplitude) to achieve all the considered scan angles. Scan angles of 0°, 30° and 60° are presented to investigate the limits of the structure. For brevity, 40° and 50° are only reported in the final comparison table in Section 4.3.

4.1. Quadridge Radiating Elements

The ARC of the open-ended quadridge waveguide reported in Section 3.1, whose parameters are summarized in Table 1, is reported in Figure 10a for linear polarization. The ARC is the relevant physical parameter because it directly accounts for both the self-reflection of the element itself and all the mutual coupling contributions from the other array elements. The ARC strongly depends on the scan angle/plane because the coupled contributions also depend on the phase shift between cells (as reported above, the phase shift is related to the scan angle). The solid, dashed and dotted lines refer to the E- ($\phi = 0°$), D- ($\phi = 45°$) and H-planes ($\phi = 90°$), respectively. The line colours identify the scanning angles. The vertical black dash-dotted lines indicate the cut-off frequencies of the waveguide and the green box highlights the operative bandwidth. The ARC for only one of the two fundamental degenerate modes is shown due to its 90° rotational symmetry along the propagation axis.

Table 1. Design parameter values for the quadridge elements.

Parameter	Description	Values (mm)
P	Period	7.8
a	Aperture side	6.8
h_R	Ridge height	1.5
w_R	Ridge width	1
l_E	Evanescent section length	1

It can be seen that the open-ended quadridge waveguide does not provide a satisfactory matching level even at the broadside (green solid line). This is related to the proximity of the lower cut-off frequency (vertical black dash-dotted line). In addition, when scanning up to 60° in the E-plane (red solid line), scan blindness is observed at 20 GHz, i.e., the signal is completely reflected at this frequency, reducing the bandwidth even further. The other principal plane (dotted red line) instead shows a reflection level of about −5 dB for the overall band.

Two sharp features on the S_{11} curves are visible above the upper limit of the frequency band. The first one, located at 20.47 GHz (vertical black dash-dotted line), is due to the higher-order mode of the waveguide. It is related to the waveguide geometry, therefore, it is independent of the scan angle. However, it does not appear at $\phi = 90°$ (dotted line) because of the symmetry of the structure, i.e., the fundamental mode is not coupled to the third mode along such a plane (H-plane). The second sharp feature is at 20.61 GHz (black arrow) and this is due instead to the appearance of the grating lobes at this frequency (see Equation (1)).

Concerning the coupling for linear polarization, it is only significant in the D-plane, where it reaches −6.5 dB when the scan angle goes up to 60°. These curves are not

shown for brevity. However, their effect is included in the circular polarization behaviour discussed hereafter.

As far as the ARC for circular polarization is concerned, scan blindness decreases by almost 3 dB (red solid line in Figure 10c) because, as stated above, only one of the two linear components is completely reflected. The results shown for circular polarization have been calculated taking into account an ideal polarizer (the parameters simulated for linear polarization have been combined according to Equations (2) and (3)).

$$S_{11}^{Circ} = \frac{1}{2}[S_{11} - S_{22} - j(S_{12} + S_{21})] \tag{2}$$

$$S_{21}^{Circ} = \frac{1}{2}[S_{21} - S_{12} - j(S_{11} + S_{22})] \tag{3}$$

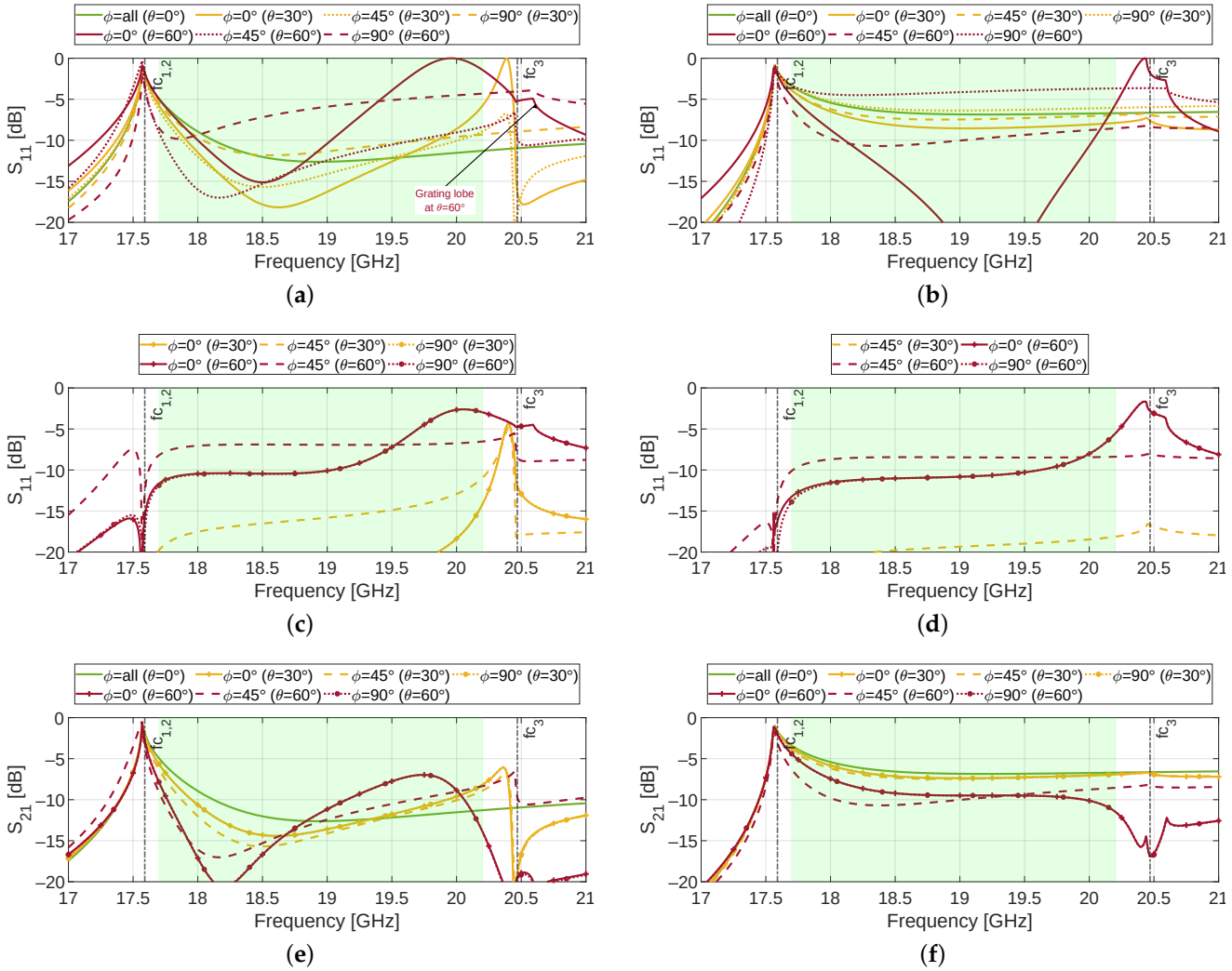

Figure 10. S-Parameters for both quadridge designs. The dashed lines indicate the cut-off frequencies and the green box indicates the operative frequency band. (**a**) Quadridge for linear polarization; (**b**) evanescent quadridge for linear polarization; (**c**) quadridge for circular polarization. S_{11} for ($\theta = 0°$) is below −20 dB; (**d**) evanescent quadridge for circular polarization. S_{11} for ($\phi = 0°/90°$, $\theta = 30°$) and ($\theta = 0°$) is below −20 dB; (**e**) quadridge for circular polarization; (**f**) evanescent quadridge for circular polarization.

To overcome this scan blindness, a square waveguide section can be placed between the end of the ridges and the aperture (see Figure 11). Its effect on the E-plane response is shown in Figure 12 as a function of the length l_E. The same phenomenon, also called spurious

resonance, has been studied in [5] considering circular polarization. Here, the impact is even more apparent for linear polarization (Figure 12), where the scan blindness is shifted to higher frequencies and then out of the band, increasing the length l_E. An optimal value of l_E, 1 mm, has been chosen to achieve the same reflection coefficient value at the two ends of the band (around -5 dB).

The whole phenomenon of the scan blindness reduction is complex because it involves a multimodal interaction between the end of the ridges and the aperture. In the quadridge-to-free space discontinuity (Figure 3), the higher-order mode of the quadridge is strongly excited on the aperture because its cut-off frequency $f_{c_3} = 20.4$ GHz is close to the upper limit of the frequency band. On the contrary, when the square waveguide section is added (Figure 11), both fundamental degenerate (TE_{10}, TE_{01}) and higher-order modes (TE_{11}, TM_{11}) are excited at the end of the ridges. However, the TE_{11} and TM_{11} are significantly attenuated (4.3 dB/mm at 20.2 GHz) because their cut-off frequency (31.1 GHz) is far from the operative bandwidth. In this way, the contribution of such higher-order modes to radiation is reduced with respect to the abrupt quadridge-free space interface. It should be mentioned that the TE_{10} is also below cut-off (about 22 GHz). Nevertheless, as shown in Figure 10b, such a slightly evanescent mode (1.6 dB/mm) does not prevent radiation. However, the overall ARC is higher (at broadside and 30°) with respect to the quadridge element (see Figure 10a). The S_{11} levels are quite acceptable for circular polarization (see Figure 10d) because (due to the polarizer) such a reflection coefficient basically depends on the difference between ARCs for the two linear polarizations, which is related to the difference response in the two orthogonal planes (see Equation (2)).

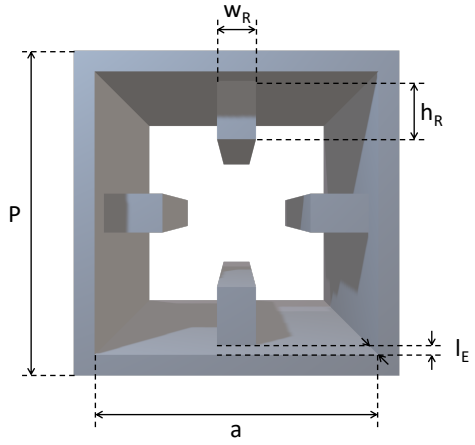

Figure 11. Evanescent quadridge waveguide geometry.

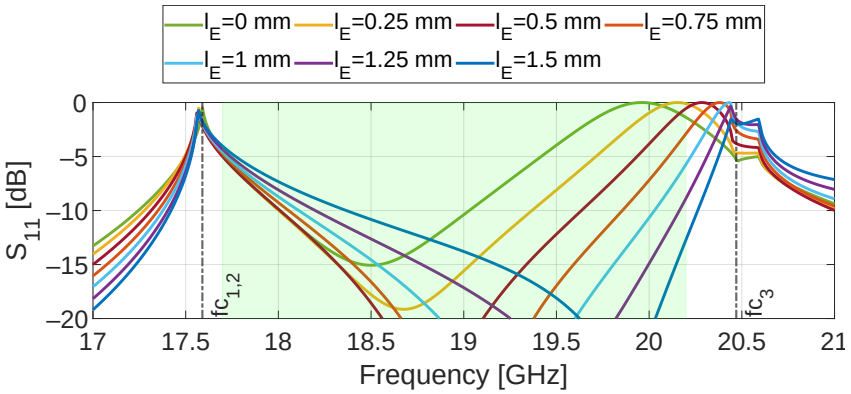

Figure 12. Scan blindness effect on the ARC depending on the evanescent length at $\phi = 0°$ and $\theta = 60°$.

A further increment in l_E will result in a lower and flatter S_{11} for circular polarization, but the S_{21} will increase when in proximity of the lower end of the bandwidth. For this reason, $l_E = 1$ mm can also be considered an optimum value for circular polarization.

As far as circular polarization is concerned, the evanescent quadridge provides an improvement of about 2–3 dB and overall bandwidth enlargement (Figure 10d) with respect to the nominal one (Figure 10c). The coupling S_{21} shows values equals to −5 dB at the lower end of the band due to the proximity of the cut-off frequency in both designs (Figure 10e,f). The impact of the increased ARC of the evanescent quadridge at low scanning angles is visible on S_{21} (about −6 dB) throughout the band.

In conclusion, the quadridge with an evanescent section, which does not show the blindness at the expense of a higher reflection coefficient for linear polarization (and higher S_{21} for circular), can be suitable for single-pol DRAs, where the port of the unexcited polarization is closed on a matched load (with a reduction in the overall efficiency).

Figure 13 shows the scan loss at the band limits and center frequency when scanning from −60° to 60° for both quadridge designs in both linear and circular polarization. The scan loss is an important figure-of-merit that quantifies the reduction in the array beam's maximum radiated power (with respect to broadside $\theta = 0$) as a function of the scan angle/plane. The circular polarization data have been computed according to Equations (4) and (6) as a function of the radiated field for linear polarization.

$$E_{co,LH} = \frac{1}{2}\left[(E_{\theta,1} + jE_{\theta,2}) - j(E_{\phi,1} + jE_{\phi,2})\right] \tag{4}$$

$$E_{cross,LH} = \frac{1}{2}\left[(E_{\theta,1} + jE_{\theta,2}) + j(E_{\phi,1} + jE_{\phi,2})\right] \tag{5}$$

$$E_{co,RH} = \frac{1}{2}\left[(E_{\theta,1} - jE_{\theta,2}) + j(E_{\phi,1} - jE_{\phi,2})\right] \tag{6}$$

$$E_{cross,RH} = \frac{1}{2}\left[(E_{\theta,1} - jE_{\theta,2}) - j(E_{\phi,1} - jE_{\phi,2})\right] \tag{7}$$

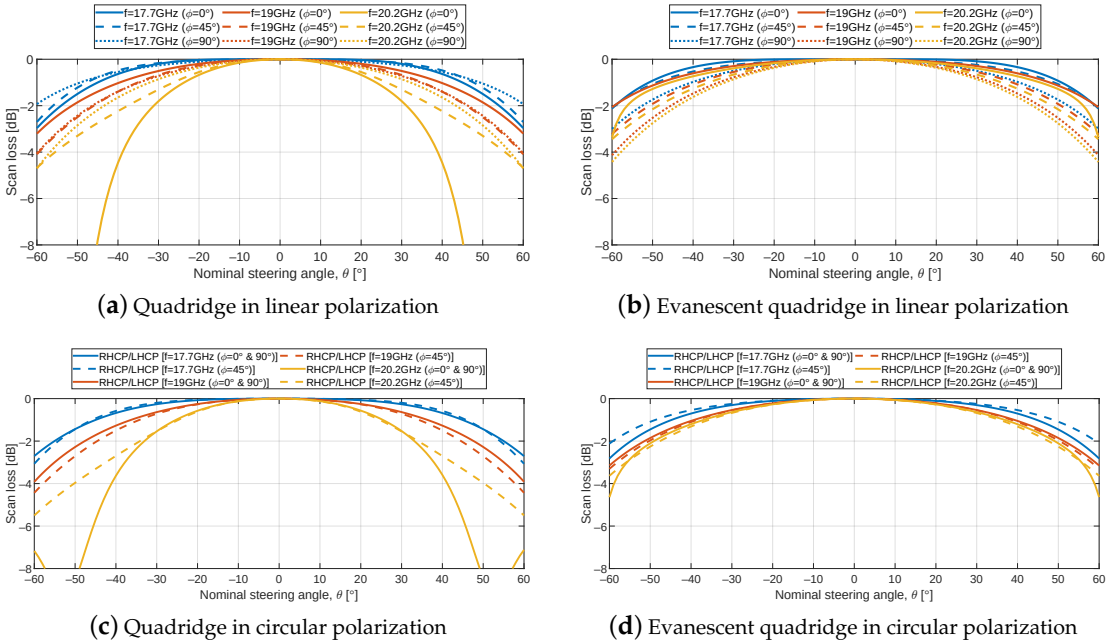

(**a**) Quadridge in linear polarization

(**b**) Evanescent quadridge in linear polarization

(**c**) Quadridge in circular polarization

(**d**) Evanescent quadridge in circular polarization

Figure 13. Scan loss for both quadridge designs.

From Figure 13a, a maximum difference of 2 dB is observed between planes at 17.7 GHz (blue lines) and 19 GHz (red lines). At 20.2 GHz (yellow lines) the scan loss drops more than 6 dB due to the scan blindness discussed above. The same consideration applies for circular polarization (Figure 13c). When the evanescent section is added (Figure 13b),

the drop due to scan blindness at the upper frequency of the band disappears, obtaining values between −2 and −4 dB for all the planes and frequencies. Similar values are visible for circular polarization.

The XPD performance in D-plane (Ludwig 3) is shown in Figure 14. This parameter quantifies the polarization purity of the array beam at the corresponding scan angle. The E- and H-planes are not reported due to the two-fold symmetry (the simulated values are above 40 dB). Circular polarization data have been computed as the ratio between the Equations (4) and (5), and Equations (6) and (7). The quadridge for linear polarization (Figure 14a) provides values around 10 dB at 17.7 and 19 GHz, and a value of about 7 dB at the upper frequency. The presence of the blindness is clearly visible for circular polarization (Figure 14c), where XPD approaches 0 dB. This happens because one of the two linear components is completely reflected and hence the radiated field is linearly polarized. The values of the scan limits improve for the evanescent quadridge, being higher than 14 dB for the three frequencies for linear polarization (Figure 14b). The values of XPD are related to both the intrinsic cross-polarization levels of the fundamental modes presented in Section 3.1 (that are non-zero in the D-plane) and the contribution of the evanescent higher-order modes excited at the aperture (discontinuity between waveguide and free-space). In terms of circular polarization (Figure 14d), there is a decrease at 20.2 GHz in the planes $\phi = 0°/90°$. This is due to the different radiation patterns for the two principal polarizations at high scan angles, as can be seen when comparing solid and dotted lines in Figure 13b (see Equations (4)–(7)).

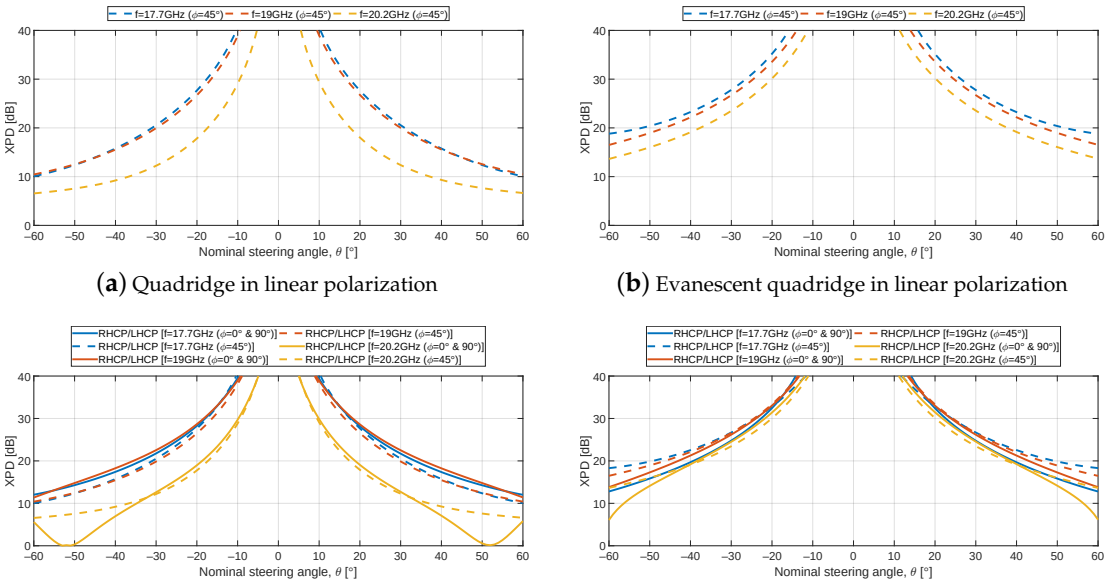

(**a**) Quadridge in linear polarization

(**b**) Evanescent quadridge in linear polarization

(**c**) Quadridge in circular polarization

(**d**) Evanescent quadridge in circular polarization

Figure 14. XPD for both quadridge designs.

4.2. Hexagonal Ridged Radiating Elements

Differently from the quadridge, where the optimum value (OV) of the ridge dimensions was selected on the basis of the cut-off analysis only, the hexagonal structures allow for a larger range of parameters (see Section 3.2). For this reason, full-wave analyses have been carried out to determine the OVs for the three and six-ridge configurations. Figure 15 shows the contour plots of ARC averaged (from broadside direction to maximum scan angle) as a function of the ridge parameters for a 5% (Figure 15a,b) and 13.2% (Figure 15c,d) bandwidth. This allows to check which ridge dimension combination provides the best starting point in terms of matching. In this case, a similar performance is obtained whether the design considers the whole band or only a percentage of it. As expected, the design curves for a 5% bandwidth provide a larger useful region in terms of parameter combina-

tions. For both configurations, where the optimal (blue) region is apparent, the selected OVs are shown in Table 2. The manufacturing constraint of 1 mm for the ridge width has also been considered. The optimum values for the hexagon with three ridges (Figure 15c) are 1 mm and 1.75 mm for width and height, respectively. The resultant cut-off frequencies are 17.4 GHz and 30.7 GHz for the fundamental and higher-order modes. In the case of six ridges (Figure 15d), optimum values are 1 mm and 1.7 mm for width and height, respectively. In this case, cut-off frequencies are 17.4 GHz and 21.7 GHz for the fundamental and higher-order modes.

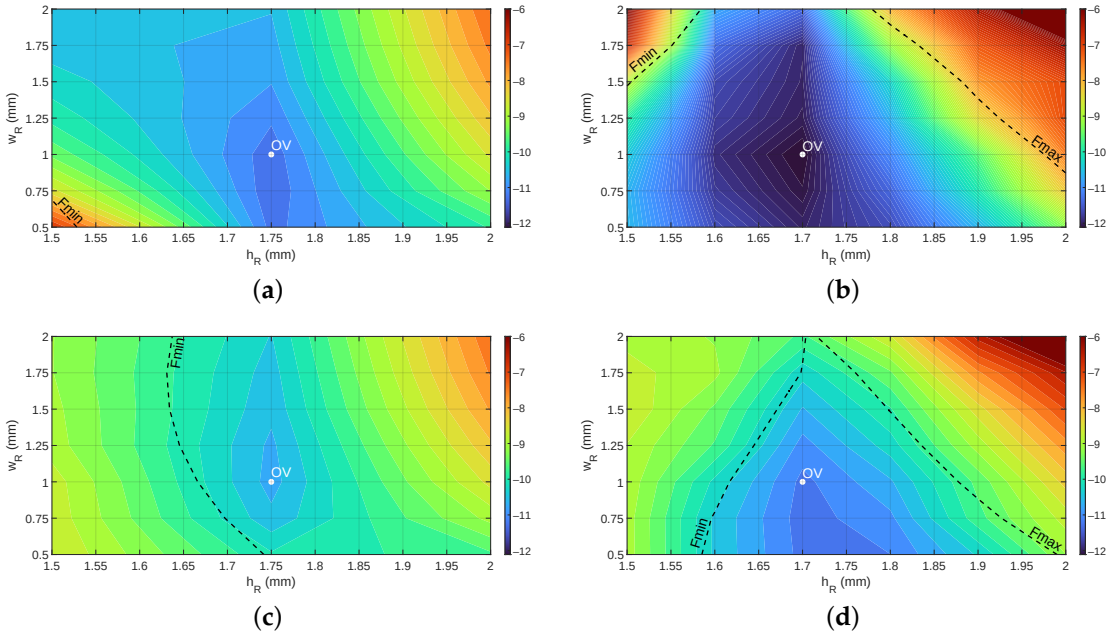

Figure 15. ARC averaged on the scan range as a function of the ridge parameters. OV indicates the optimum value based on the manufacturing constraints. (**a**) Hexagon with three ridges in a 5% bandwidth; (**b**) hexagon with six ridges in a 5% bandwidth; (**c**) hexagon with three ridges in a 13.2% bandwidth; and (**d**) hexagon with six ridges in a 13.2% bandwidth.

The S-Parameters of both hexagonal designs in the E-, D- and H-planes at different scan angles are reported in Figure 16a,b. No scan blindness is visible due to the high cut-off frequency of the third mode. The worst value is around −4 dB in the H-plane when scanning to the 60° limit (dotted red line). For smaller scan angles (green and yellow lines), the six-ridge solution provides an improvement of about 2 dB in the E- and D-planes above 18.5 GHz. Scattering parameters for the other fundamental mode (S_{22}, i.e., the other polarization) are similar to S_{11}, therefore they are not reported for brevity. S_{21} for linear polarization (not shown) is in the order of −10 dB and its effect is accounted for in the circular polarization data.

Table 2. Design parameter values for the ridged hexagonal apertures.

Parameter	Description	Values (mm)
P	Period	9
a	Aperture side	8
h_{R1}	Ridge height (three ridges)	1.75
w_{R1}	Ridge width (three ridges)	1
h_{R2}	Ridge height (six ridges)	1.7
w_{R2}	Ridge width (six ridges)	1

As far as circular polarization is concerned, both hexagonal designs (Figure 16c,d) have similar behaviours. The three-ridge solution has a flatter behaviour due to the higher cut-off frequency of the third mode. The overall levels are similar to the evanescent quadridge in Figure 10d. The coupling for circular polarization for the hexagon with three ridges is shown in Figure 16e. The values are below -10 dB for scanning angles up to 30° for each principal plane. A value of about -5 dB is obtained at the scanning angle limit for $\phi = 90°$ (dotted red line). Comparing Figure 16c,d, it can be observed that the six-ridge solution exhibits a worse performance at the upper frequency limit of the band (i.e., some bandwidth reduction). Again, this is due to the lower cut-off frequency of the higher-order mode (21.7 GHz) with respect to the three-ridge counterpart (30.7 GHz). Similar values are obtained for the coupling for circular polarization of the six-ridge configuration in (Figure 16f). In this case, there is less variations between the planes. The worst value is obtained at 60° for $\phi = 90°$ (dotted red line), being -5 dB at higher frequencies.

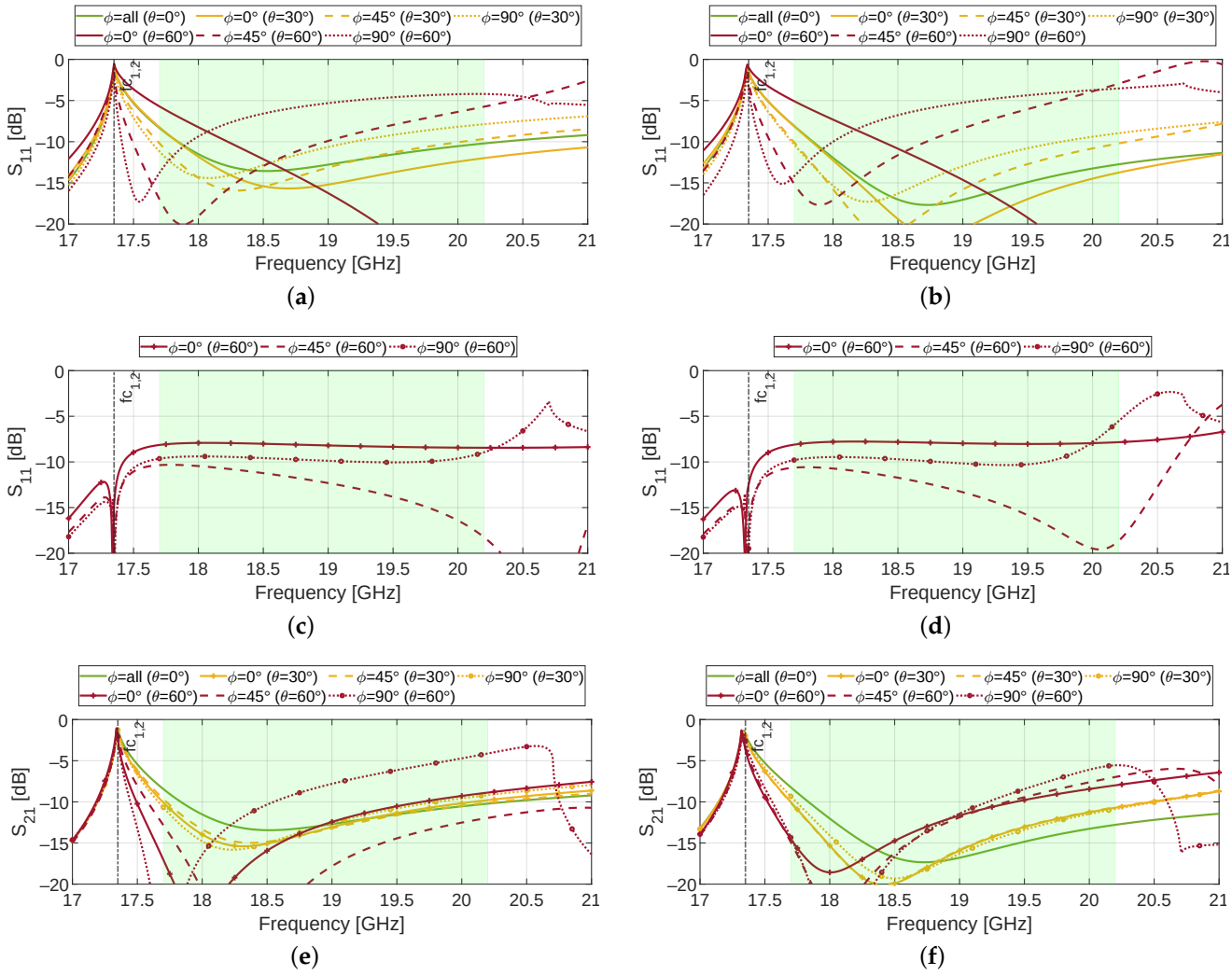

Figure 16. S-Parameters for both hexagonal designs. The dashed lines indicate the cut-off frequencies and the green box indicates the operative frequency band. (**a**) Hexagon with three ridges for linear polarization; (**b**) hexagon with six ridges for linear polarization; (**c**) hexagon with three ridges for circular polarization. S_{11} for ($\theta = 0°/30°$) is below -20 dB; (**d**) hexagon with six ridges for circular polarization. S_{11} for ($\theta = 0°/30°$) is below -20 dB; (**e**) hexagon with three ridges for circular polarization; and (**f**) hexagon with six ridges for circular polarization.

Concerning the scan loss, Figure 17 shows the results of both hexagonal designs within the scan range of $-60°$ to 60° for both linear and circular polarization. In terms of linear

polarization, both hexagonal apertures (Figure 17a,b) show a decay between 2.5 and 3.5 dB at $\pm 60^\circ$ in the E-plane for the three considered frequencies (solid lines). These values increase up to 5 dB for the hexagonal aperture with three ridges and up to 6 dB for the hexagonal aperture with six ridges, in both D- and H-planes (dashed and dotted lines).

Differently from the quadridge structure, the hexagonal waveguide apertures do not have 90° rotational symmetry. Therefore, a full set of scan losses and XPD data is provided for both left-hand (LH) and right-hand (RH) circular polarization. For both solutions, the scan loss ranges from 3 to 6 dB (Figure 17c,e). Minor differences are visible between the two circular polarizations.

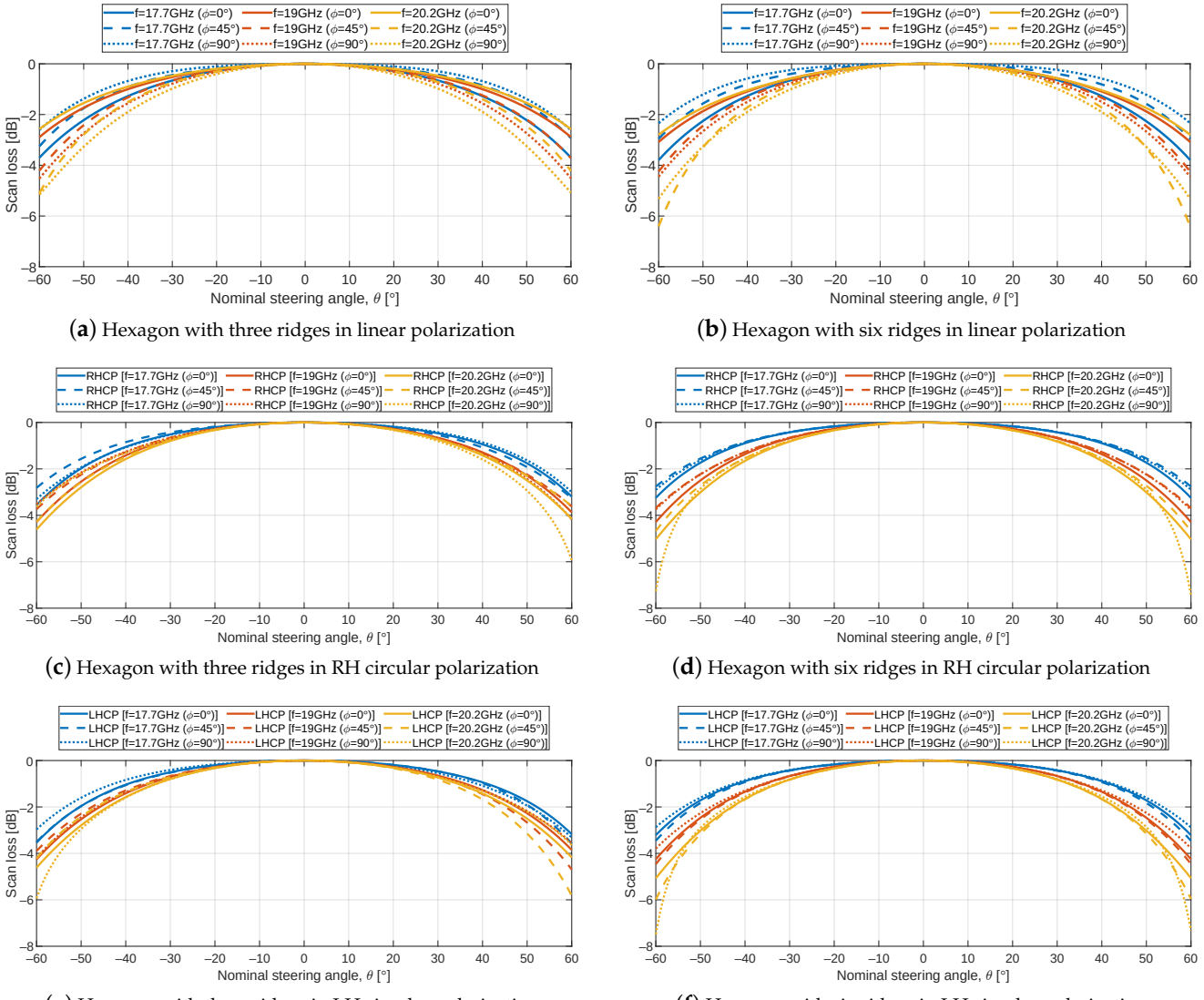

(**a**) Hexagon with three ridges in linear polarization

(**b**) Hexagon with six ridges in linear polarization

(**c**) Hexagon with three ridges in RH circular polarization

(**d**) Hexagon with six ridges in RH circular polarization

(**e**) Hexagon with three ridges in LH circular polarization

(**f**) Hexagon with six ridges in LH circular polarization

Figure 17. Scan loss for both hexagonal designs.

The XPD is reported in Figure 18. The curves for the three-ridged aperture are not symmetrical along the scan range (Figure 18a,c,e) due to the one-fold symmetry of the geometry (the same consideration applies for the scan loss in Figure 17a,c,e). Symmetrical curves with respect to broadside ($\theta = 0$) are instead observed for the six-ridge solution thanks to its two-fold symmetry. XPD values ranging from 8 to 10 dB are observed at the scan limits. As already discussed for the quadridge, these values are related to the different behaviour of the structure for the two principal polarizations along the scan planes. It should be noted that the complete scan loss and polarization analyses reported in

Figures 17 and 18 are required to appreciate the performance variation along the various planes for both polarizations and asses the worst cases.

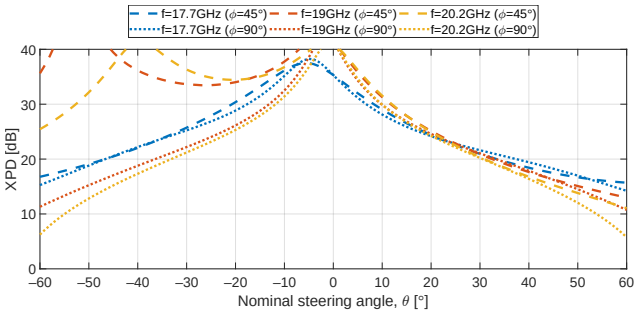

(**a**) Hexagon with three ridges in linear polarization

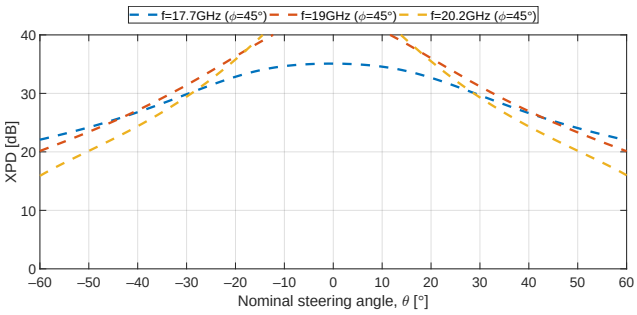

(**b**) Hexagon with six ridges in linear polarization

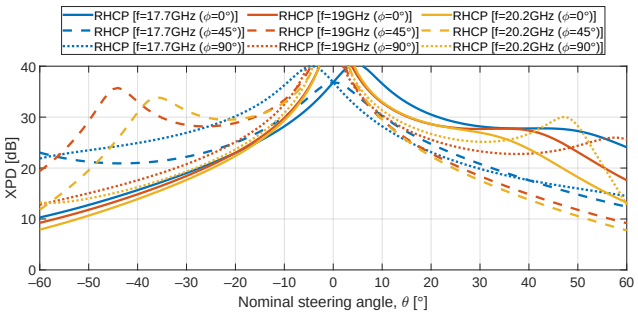

(**c**) Hexagon with three ridges in RH circular polarization

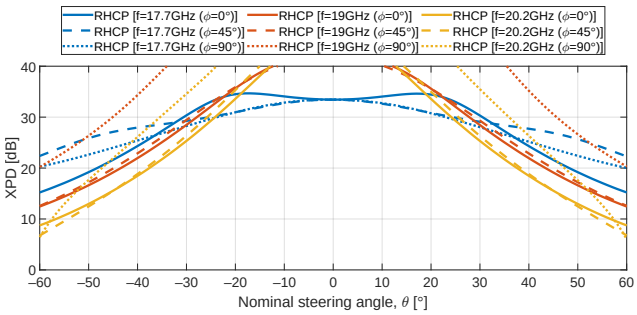

(**d**) Hexagon with six ridges in RH circular polarization

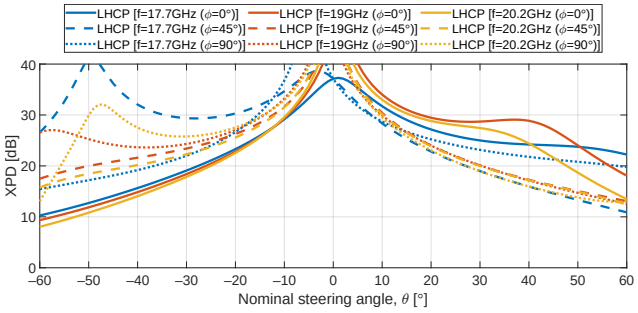

(**e**) Hexagon with three ridges in LH circular polarization

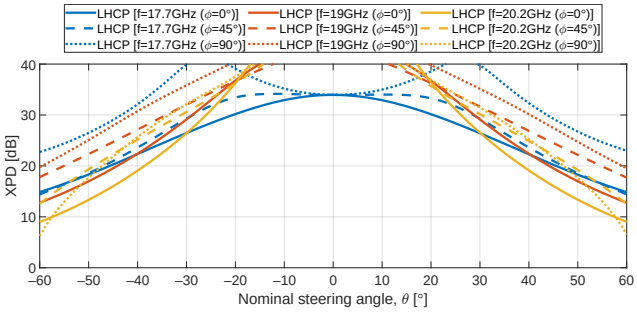

(**f**) Hexagon with six ridges in LH circular polarization

Figure 18. XPD for both hexagonal designs.

4.3. Performance Comparison

A brief summary comparing the different structures for ARC, scan loss and XPD is shown in Figure 19.

The reflection coefficient and the coupling are reported in Figure 19a–c for circular polarization. The line colours refer the different apertures, the line type the scanning angles and the green box highlights the operative bandwidth.

The quadridge without an evanescent section has been reported for completeness. However, it is apparent that the scan blindness impairs the overall performance in terms of reflection (−4 dB) for high scan angles (Figure 19a, blue line). The evanescent quadridge instead provides an improvement, displacing the high reflection outside the band (see Figure 19a, red line, −5 dB at 20.2 GHz).

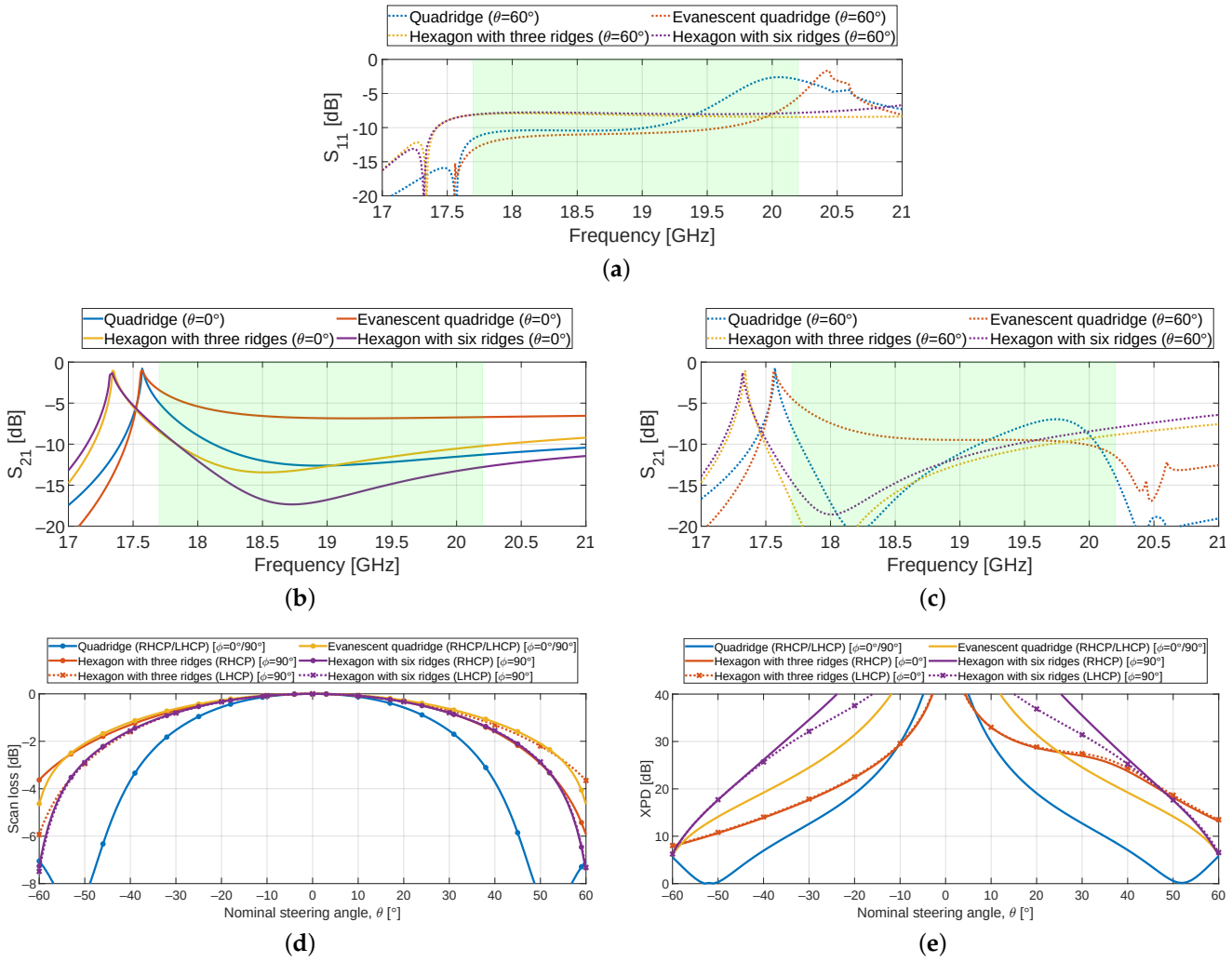

Figure 19. Comparison of ARC, scan loss and XPD for all analysed apertures for circular polarization. (**a**) S_{11} at scan angle limit. The green box indicates the operative frequency band; (**b**) S_{21} at broadside. The green box indicates the operative frequency band; (**c**) S_{21} at scan angle limit. The green box indicates the operative frequency band; (**d**) scan loss at 20.2 GHz; (**e**) XPD at 20.2 GHz.

Concerning to the coupling at the broadside (Figure 19b), the hexagon aperture shows an improvement of 6 (yellow line) and 10 dB (purple line) with respect to the evanescent quadridge (red line) at the central frequency when it is loaded with three and six ridges, respectively. Instead, for high scan angles (Figure 19c), both hexagon apertures have a similar trend up to 1 dB of difference between them.

Figure 19d,e shows the scan loss and XPD, respectively, at the highest frequency of the band, 20.2 GHz, when scanning from $-60°$ to $60°$ for the circular polarization for all apertures. Values of 8 and 0 dB for the high scan angles are obtained for the quadridge in both scan loss and XPD, respectively. The evanescent quadridge (yellow line) shows a stable and uniform scan loss for both the right and left circular polarization with a drop of 2 dB within a 13.2% bandwidth up to a $50°$ scan angle. In terms of XPD, values of 14 dB are obtained. Acceptable values have been obtained for the scan loss in both hexagonal apertures (-3 dB) scanning up to $50°$ (red and purple lines). Instead, the hexagon with six ridges shows better performance in terms of XPD than the other apertures, with values better than 18 dB when it scans up to $50°$.

The performances of the proposed designs are listed in Table 3. The scan angle of $40°$ and $50°$ are also reported to provide direct comparison to the literature data. All the data refer to circular polarization.

Reference [5] reports an EQA with a matching section providing acceptable reflection and coupling up to ±50° within a bandwidth of 4.5% (simulated data). The worst case XPD level is only 8 dB.

For the radiated elements presented in this work, no matching section is included. In this way, the reported data show the intrinsic performance of such radiating apertures (open-ended waveguides), i.e., the performance that can be achieved with minimum complexity. The reported data can be used as a reference for the future design of more complex elements including matching discontinuities.

The performance for scan angles of 60° is not satisfactory for all the elements. The coupling is above −10 dB even at 50° scan angles. From these considerations, we can conclude that such elements can be suitable for single polarized DRAs (which, to the best of the author's knowledge are the configurations currently being adopted for LEO satellites) operating up to 50° scan angles, when the unexcited port is closed on a matched load. This will reduce the element radiation efficiency. However, it will provide a smooth frequency response (without spurious resonances/spikes).

Table 3. Performance comparison between proposed designs. All the data refer to circular polarization.

Radiating Element	Lattice	BW (%)	Scan Angle, θ (°)	S_{11} (dB)	S_{21} (dB)	Scan Loss (dB)	XPD (dB)
Evanescent quadridge [5]	Square	4.5	0	−40	−12	-	40
			30	−15	−13	1	15
			40	−12	−9	1	10
			50	−10	−6	2	8
			60	NA	NA	NA	NA
	Square	13.2	0	−53	−4	-	40
			30	−11	−6	2	12
			40	−9	−6	2	7
			50	−4	−6	8	0
			60	−3	−7	7	6
	Square	13.2	0	−41	−3	-	40
			30	−18	−4	1	23
			40	−14	−4	1	19
			50	−11	−4	2	14
			60	−6	−4	4	6
	Triangular	13.2	0	−35	−8	-	40
			30	−21	−9	1	18
			40	−15	−8	2	14
			50	−11	−6	3	11
			60	−8	−4	6	8
	Triangular	13.2	0	−31	−8	-	40
			30	−21	−9	1	25
			40	−14	−9	2	18
			50	−10	−8	3	12
			60	−6	−6	7	6

5. Comparison between Infinite and Finite Approaches

The results reported in this paper have been computed at the aperture level with an infinite array approach. As far as the aperture full-wave analysis in a periodic environment is concerned, the critical aspects are related to the high number of required modes in the Floquet ports to allow for proper field absorption at high scan angles and to the significant performance variation (mainly ARC) observed in Section 4. The latter is the relevant characteristic that requires validation. We know that experimental verification is the final goal for fully independent verification, however, it would require the design and manufacturing of polarizers [26], launchers and, in general, matching sections. Such components will

add additional design parameters and uncertainties in the overall verification process. Moreover, the experimental validation should be performed by implementing a finite array with either a reconfigurable BFN or additional post-processing to achieve ARC, scan loss and XPD from measurements at the element level (scattering matrices and embedded element patterns). Both BFN and such post-processing methods would introduce additional uncertainties in the overall verification process.

All these considerations led us to the full-wave analyses on finite structures reported in this section. Convergence of such finite array results is assessed by varying both the number of elements and the distance between the structure and the boundary conditions. This analysis is also useful to assess the minimum number of elements that should be considered for array prototyping. Provided that there is good agreement between the infinite and finite array approaches, there are several papers demonstrating good agreement between simulations and measurements in finite arrays (see, for example, [7,9]). As far as metal waveguide components are concerned, we already compared the adopted full-wave software with measurements up to W-band in previous papers (see, for example, [26,31]).

Two relevant configurations have been selected, i.e., the quadridge in the square lattice and the hexagon with three ridges in the triangular lattice. The quadridge is significant because of its scan blindness. The hexagon with three ridges is interesting because of its one-fold symmetry and the triangular lattice arrangement. The validation has been carried out comparing three sets of results: an infinite approach (unit cell) in both CST Studio Suite 2021 and HFSS 2022, and a finite array simulation in CST.

For the hexagonal structure, a simple transition with two steps from a smaller waveguide to the aperture has been introduced to avoid overlapping the waveguide ports in the finite array configuration. The same transition has also been included in the infinite simulation for consistency. Therefore, the presented results are slightly different from the ones presented in Section 4.2.

In the infinite approach, a Floquet port has been used instead of the perfect matched layer (PML) because it provides better absorption at higher scan angles [32]. Up to 18 Floquet modes have been considered in both lattices for CST. The number of modes in HFSS has instead been increased to 30 and 42 for the square and triangular lattice, respectively, to achieve an attenuation of 50 dB for the last considered mode [33]. In both infinite models, the distance between the Floquet port and the aperture has been set to $0.25\lambda_0$ at 17 GHz. Both the S-Parameters for ARC and the active element pattern (AEP) for the scan loss and XPD were computed with both simulators.

The unit cell has been replicated in both directions to obtain a finite array model. PML boundary conditions have been applied at a certain distance from the model in all directions including the back. Both the number of elements and the PML distance will be discussed in the convergence analysis reported hereafter. Regarding the S-Parameters, the calculation of the ARC has been performed by summing the self-contribution of the central element and the coupling from all the other ones with the required weight for beam scanning [34]. The excitation of the central element has been considered to compute the embedded element pattern (EEP). This approach has been preferred over the scan of the whole finite array due to the limited number of elements in a row/column.

Figure 20a,b show the convergence analysis of the finite array model and its comparison to the infinite CST one. The most critical condition is $\theta = 60^\circ$ where the scan blindness is present at about 20 GHz for the quadridge in the square lattice. This phenomenon is difficult to model with a small finite array simulation where the contribution of the farther elements is missing. Nevertheless, both the red and cyan dashed curves (11×11 and 13×13, respectively) approach the purple curve (infinite) quite well. The convergence analysis stopped at 13×13 elements due to peak memory (150 GB) and time consumptions (9 h in a Intel Xeon with two processors at 3 GHz). It can be observed that it is not only necessary to increase the number of elements, but also the PML distance (see yellow and red dashed curves where the PML distance is 0.25λ and 1.5λ, respectively, at 17 GHz) to

achieve convergence between the finite and infinite simulations. Such distance is required to attenuate the evanescent wave interaction occurring at high scan angles.

Figure 21 shows the ARC for the E-plane ($\phi = 0°$) for both considered designs using the three simulation methods described above. For the quadridge (Figure 21a), the infinite models are in very good agreement at all scan angles. The finite array simulation (11×11) follows the same trend but with the expected discrepancy at 20 GHz. As for the hexagonal waveguide (Figure 21b), the larger differences occur when the reflection level of the infinite array is below -15 dB. An overall agreement is achieved between the curves, confirming that the results are consistent. This analysis is also useful to assess the minimum number of elements that should be considered for array prototyping. This number is smaller than 48×48 which was discussed in Section 2.

Figure 22 shows the scan loss across the D-plane at three frequencies ranging from 17.7 GHz to 20.2 GHz within a $\pm 60°$ scan angle. The three different methods are presented with solid, dashed and dotted curves (see legend). A remarkable agreement is visible for both designs.

A similar comparison is provided for the XPD in Figure 23. Good agreement between the three methods has been achieved for the quadridge. As far as the hexagonal structure is concerned, the infinite methods are in perfect agreement. The finite method shows a consistent trend. However, a significant ripple is visible on such an EEP. Additional simulation efforts should be carried out to achieve a higher degree of convergence.

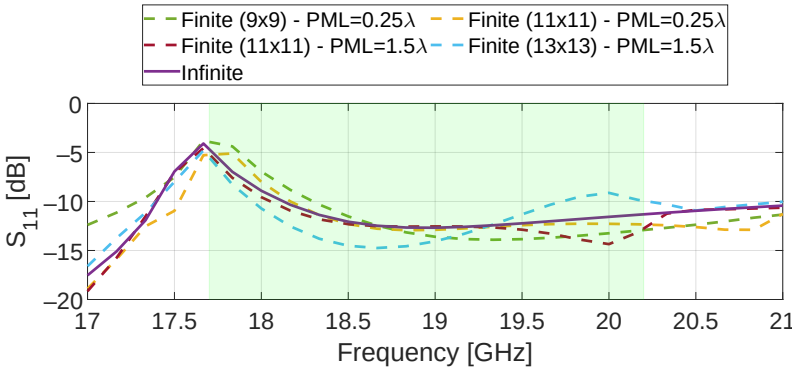

(**a**) ARC convergence at $\phi = 0°$ and $\theta = 0°$ in linear polarization

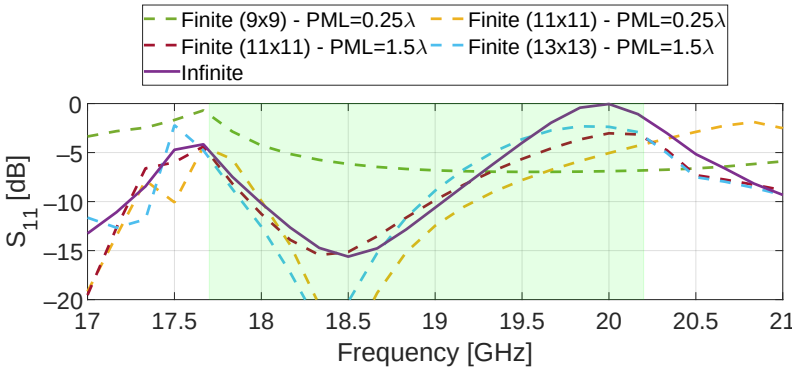

(**b**) ARC convergence at $\phi = 0°$ and $\theta = 60°$ in linear polarization

Figure 20. Effect of the number of radiating elements and PML distance for the converge of the finite array against an infinite approach.

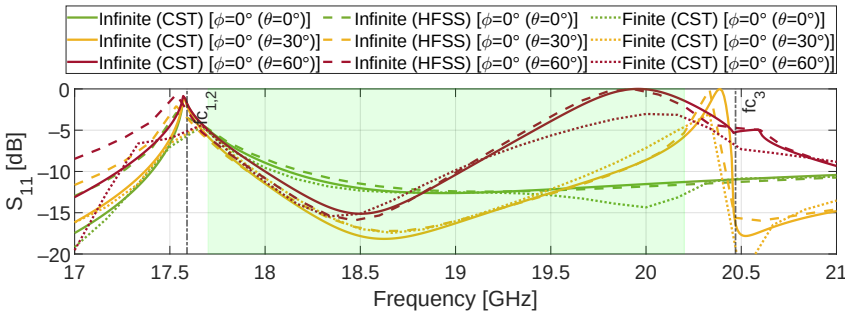

(**a**) Quadridge in linear polarization

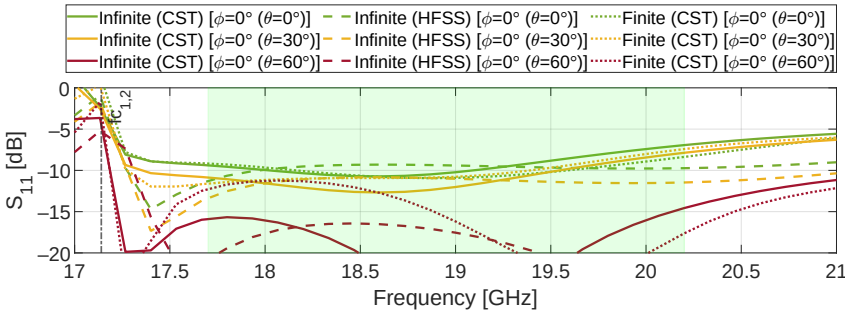

(**b**) Hexagon with three ridges in linear polarization

Figure 21. ARC convergence analysis between infinite approaches in CST and HFSS and a finite array simulation in CST. The green box indicates the operative frequency band.

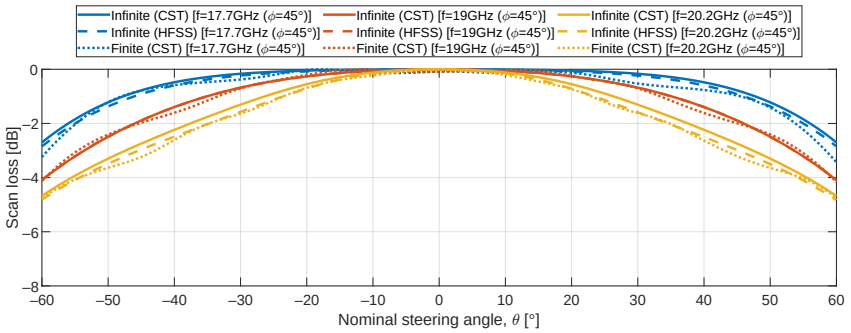

(**a**) Quadridge in linear polarization

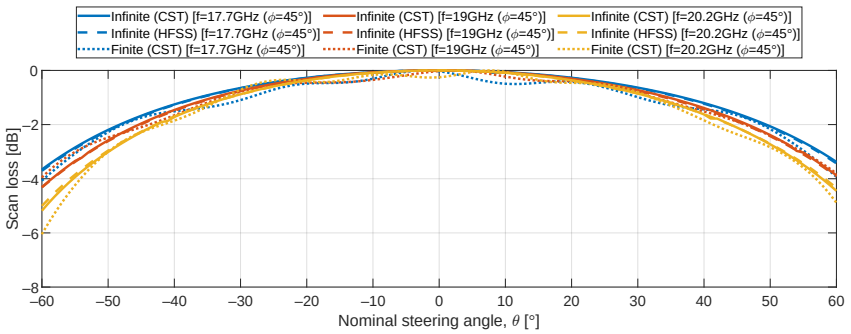

(**b**) Hexagon with three ridges in linear polarization

Figure 22. Scan loss convergence analysis between infinite approaches in CST and HFSS and a finite array simulation in CST.

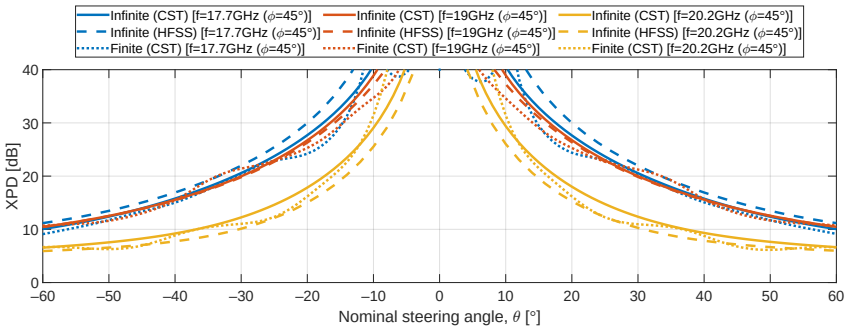

(**a**) Quadridge in linear polarization

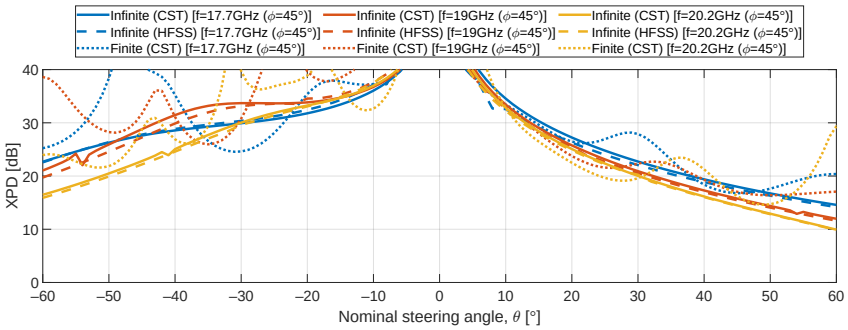

(**b**) Hexagon with three ridges in linear polarization

Figure 23. XPD convergence analysis between infinite approaches in CST and HFSS and a finite array simulation in CST.

6. Conclusions

This work studied ridged waveguide aperture (i.e., open-ended waveguide elements) solutions as array radiating elements for Ka-band downlink (relative bandwidth 13.2%). Both cut-off and full-wave parametrical analyses have been carried out to find the optimal design parameters for each structure. ARC, coupling, scan loss and XPD have been determined for both linear and circular polarizations. The impact of cut-off frequencies on the achievable element bandwidth, the presence of blindness and the effect of the structure symmetry on the radiation pattern have been discussed. The validity of the results has been verified by comparing finite and infinite approaches in both CST and HFSS.

Good performance has been achieved for both square and triangular lattices with the evanescent quadridge and three/six-ridge hexagonal waveguides, respectively. All elements show limitations in terms of coupling at high scan angles. Therefore, they will be more suitable for single-polarized DRAs operating up to 50° scan angles, with a consequent slight reduction in radiation efficiency due to the power dissipated on the matched load at the unexcited port. In this configuration, they will still provide a smooth frequency response (without spurious resonances/spikes).

Future research on this topic includes the design of suitable transitions/discontinuities for better matching across the full scan angle. Moreover, modifications of the radiating aperture to improve both XPD and coupling should be investigated to achieve high-performance dual-polarized DRAs.

Author Contributions: Conceptualization, G.V.; data curation, C.V.-S. and R.M.-R.; formal analysis, C.V.-S. and R.M.-R.; funding acquisition, G.V.; investigation, G.A., O.A.P. and G.V.; methodology, G.A., O.A.P. and G.V.; project administration, G.V.; resources, O.A.P.; software, G.A.; supervision, G.A. and G.V.; validation, G.A., O.A.P. and G.V.; visualization, C.V.-S. and R.M.-R.; writing—original draft preparation, C.V.-S. and R.M.-R.; writing—review and editing, G.A., O.A.P. and G.V. All authors have read and agreed to the published version of the manuscript.

Funding: Funded by the European Union, under ANTERRA 101072363 HORIZON-MSCA-2021-DN-01. Views and opinions expressed are however those of the author(s) only and do not necessarily reflect

those of the European Union. Neither the European Union nor the granting authority can be held responsible for them.

Institutional Review Board Statement: Not applicable.

Informed Consent Statement: Not applicable.

Data Availability Statement: The raw data supporting the conclusions of this article will be made available by the authors on request.

Conflicts of Interest: The authors declare no conflicts of interest.

Abbreviations

The following abbreviations are used in this manuscript:

LEO	Low Earth Orbit
LoS	Line of Sight
SatCom	Satellite Communications
DRA	Direct Radiating Array
EQA	Evanescent Quadridge Antenna
ARC	Active Reflection Coefficient
XPD	Cross-Polar Discrimination
BFN	Beamforming network
TE	Transverse Electric
TM	Transverse Magnetic
RH	Right Hand
LH	Left Hand
PML	Perfect Matched Layer
AEP	Active Element Pattern
EEP	Embedded Element Pattern

References

1. Giordani, M.; Zorzi, M. Non-Terrestrial Networks in the 6G Era: Challenges and Opportunities. *IEEE Netw.* **2021**, *35*, 244–251. [CrossRef]
2. Rao, S.K. Advanced Antenna Technologies for Satellite Communications Payloads. *IEEE Trans. Antennas Propag.* **2015**, *63*, 1205–1217. [CrossRef]
3. Lafond, J.C.; Vourch, E.; Delepaux, F.; Lepeltier, P.; Bosshard, P.; Dubos, F.; Feat, C.; Labourdette, C.; Navarre, G.; Bassaler, J.M. Thales Alenia Space multiple beam antennas for telecommunication satellites. In Proceedings of the 8th European Conference on Antennas and Propagation (EuCAP), The Hague, The Netherlands, 6–11 April 2014.
4. Araniti, G.; Iera, A.; Pizzi, S.; Rinaldi, F. Toward 6G Non-Terrestrial Networks. *IEEE Netw.* **2022**, *36*, 113–120. [CrossRef]
5. Polo-López, L.; Menargues, E.; Capdevila, S.; Toso, G.; García-Vigueras, M. Solving Sub-Wavelength Lattice Reduction in Full-Metal Front-Ends for Dual-Polarized Active Antennas. *IEEE Trans. Antennas Propag.* **2022**, *70*, 7413–7426. [CrossRef]
6. Vásquez-Peralvo, J.A.; Querol, J.; Ortíz, F.; Rios, J.L.G.; Lagunas, E.; Baeza, V.M.; Fontanesi, G.; Garcés-Socorrás, L.M.; Duncan, J.C.M.; Chatzinotas, S. Flexible Beamforming for Direct Radiating Arrays in Satellite Communications. *IEEE Access* **2023**, *11*, 79684–79696. [CrossRef]
7. Liang, X.; Zhang, Z.; Zeng, J.; Guan, F.; Liu, X.; Zi, J. Scan Blindness Free Design of Wideband Wide-Scanning Open-Ended Waveguide Phased Array. *IEEE Access* **2021**, *9*, 68127–68138. [CrossRef]
8. Kähkönen, H.; Ala-Laurinaho, J.; Viikari, V. A Modular Dual-Polarized Ka-Band Vivaldi Antenna Array. *IEEE Access* **2022**, *10*, 36362–36372. [CrossRef]
9. Kindt, R.W.; Logan, J.T. Benchmarking Ultrawideband Phased Antenna Arrays: Striving for Clearer and More Informative Reporting Practices. *IEEE Antennas Propag. Mag.* **2018**, *60*, 34–37. [CrossRef]
10. Barka, A.; Cabral, A.D.O.; Dorlé, A. Manufacture and Measurement of Circularly Polarized Ka-Band Radiating Elements for SatCom Wide-Angle Phased Arrays Tiles. In Proceedings of the 2023 IEEE-APS Topical Conference on Antennas and Propagation in Wireless Communications (APWC), Venice, Italy, 9–13 October 2023.
11. Gorski, P.; Vigano, M.C.; del Rio, D.L. Developments on phased array for low-cost, high frequency applications. In Proceedings of the 2017 11th European Conference on Antennas and Propagation (EUCAP), Paris, France, 19–24 March 2017.
12. Jaschke, T.; Mitto, H.K.; Jacob, A.F. An SIW fed dual-band and dual-polarized lens antenna at K/Ka-band. In Proceedings of the 2017 47th European Microwave Conference (EuMC), Nuremberg, Germany, 10–12 October 2017.
13. Montgomery, J. Ridged waveguide phased array elements. *IEEE Trans. Antennas Propag.* **1976**, *24*, 46–53. [CrossRef]

14. Radiofrequency Module, by SWISSTO12 SA and E. Menargues Gomez. (5 December 2019). European Patent EP3804023A1 [Online]. Available online: https://worldwide.espacenet.com/patent/search/family/065023945/publication/EP3804034A1?q=EP3804034A1 (accessed on 28 June 2024).
15. Montoya-Roca, R.; Vazquez-Sogorb, C.; Virone, G.; Addamo, G. Array Elements for LEO SatCom Payloads. In Proceedings of the 2023 IEEE Conference on Antenna Measurements and Applications (CAMA), Genoa, Italy, 15–17 November 2023.
16. Vazquez-Sogorb, C.; Montoya-Roca, R.; Addamo, G.; Peverini, O.; Virone, G. Multi-Beam Arrays for Future LEO SatCom Payloads. In Proceedings of the 2024 18th European Conference on Antennas and Propagation (EuCAP), Glasgow, UK, 17–22 March 2024.
17. Menargues, E.; García-Vigueras, M.; Capdevila, S.; Angeletti, P.; Toso, G. Meandered Waveguides for Active Antennas. In Proceedings of the 15th European Conference on Antennas and Propagation (EuCAP), Dusseldorf, Germany, 22–26 March 2021.
18. Antenna Source for an Array Antenna with Direct Radiation, Radiating Panel and Antenna Comprising a Plurality of Antenna Sources by THALES SA, T. Girard, M. Etcharren and A. Cot. (2022, Jun. 15). European Patent EP4012834A1 [Online]. Available online: https://worldwide.espacenet.com/patent/search/family/075850247/publication/EP4012834A1?q=EP4012834A1 (accessed on 28 June 2024).
19. Dicandia, F.A.; Genovesi, S. Exploitation of Triangular Lattice Arrays for Improved Spectral Efficiency in Massive MIMO 5G Systems. *IEEE Access* **2021**, *9*, 17530–17543. [CrossRef]
20. Haupt, R.L. Array Factor Analysis. In *Antenna Arrays: A Computational Approach*; Wiley-IEEE Press: Hoboken, NJ, USA, 2010.
21. Addamo, G.; Peverini, O.A.; Calignano, F.; Manfredi, D.; Paonessa, F.; Virone, G.; Dassano, G. 3-D Printing of High-Performance Feed Horns from Ku- to V-Bands. *IEEE Antennas Wirel. Propag. Lett.* **2018**, *17*, 2036–2040. [CrossRef]
22. Anderson, T.N. Rectangular and Ridge Waveguide. *IRE Trans. Microw. Theory Tech.* **1956**, *4*, 201–209. . [CrossRef]
23. Helszajn, J. The ridge waveguide. In *Ridge Waveguides and Passive Microwave Components*; Electromagnetic Waves; Institution of Engineering and Technology: Stevenage , UK, 2000; pp. 1–12.
24. Sirci, S.; Menargues, E.; Billod, M. Space-qualified Additive Manufacturing and its Application to Active Antenna Harmonic Filters. In Proceedings of the IEEE MTT-S International Microwave Filter Workshop (IMFW), Perugia, Italy, 17–19 November 2021.
25. Dassault Systemes. CST Studio Suite: High Frequency Simulation. Available online: https://space.mit.edu/RADIO/Documentation/CST%20Studio%20Suite%20-%20High%20Frequency%20Simulation.pdf (accessed on 28 June 2024).
26. Addamo, G.; Peverini, O.A.; Manfredi, D.; Calignano, F.; Paonessa, F.; Virone, G.; Tascone, R.; Dassano, G. Additive Manufacturing of Ka-Band Dual-Polarization Waveguide Components. *IEEE Trans. Microw. Theory Tech.* **2018**, *66*, 3589–3596. [CrossRef]
27. Sun, W.; Balanis, C.A. Analysis and design of quadruple-ridged waveguides. *IEEE Trans. Microw. Theory Tech.* **1994**, *42*, 2201–2207. [CrossRef]
28. Peverini, O.A.; Addamo, G.; Virone, G.; Tascone, R.; Orta, R. A Spectral-Element Method for the Analysis of 2-D Waveguide Devices with Sharp Edges and Irregular Shapes. *IEEE Trans. Microw. Theory Tech.* **2011**, *59*, 1685–1695. [CrossRef]
29. Radiofrequency Component Having a Plurality of Waveguide Devices Provided with Ridges, by SWISSTO12 SA, E. Menargues Gomez, T. Debogovic, S. Capdevila Cascante and E. De Rijk. (2020, Oct. 01). European Patent EP3824511A1 [Online]. Available online: https://worldwide.espacenet.com/patent/search/family/067441407/publication/EP3824511A1?q=EP3824511A1 (accessed on 28 June 2024).
30. Orta, R.; Savi, I.P.; Tascone, R. Numerical Green's function technique for the analysis of screens perforated by multiply connected apertures. *IEEE Trans. Antennas Propag.* **1996**, *44*, 765–776. [CrossRef]
31. Virone, G.; Peverini, O.A.; Lumia, M.; Farooqui, M.Z.; Addamo, G.; Tascone, R. W-Band Orthomode Transducer for Dense Focal-Plane Clusters. *IEEE Microw. Wirel. Components Lett.* **2015**, *25*, 85–87. [CrossRef]
32. Bhattacharyya, A. Introduction to Floquet Modes in Infinite Arrays. In *Phased Array Antennas: Floquet Analysis, Synthesis, BFNs, and Active Array Systems*; Wiley-Interscience; John Wiley & Sons, Inc.: Hoboken, NJ, USA, 2006; pp. 61–83.
33. ANSYS, Inc. Getting Started with HFSS: Floquet Ports. Release 2020 R2—July 2020. Available online: https://www.oldfriend.url.tw/Tutorials/Ansoft/hfss/HFSS%20Floquet%20Ports.pdf (accessed on 28 June 2024).
34. Bhattacharyya, A. Finite Array Analysis Using Infinite Array Results: Mutual Coupling Formulation. In *Phased Array Antennas: Floquet Analysis, Synthesis, BFNs, and Active Array Systems*; Wiley-Interscience; John Wiley Sons, Inc.: Hoboken, NJ, USA, 2006; pp. 129–135.